

Time-resolved imaging of optical coefficients through murine chest cavities

Mark J. Niedre

Gordon M. Turner

Vasilis Ntziachristos

Massachusetts General Hospital

Harvard Medical School

Laboratory for Bio-Optics and Molecular Imaging

Center for Molecular Imaging Research

Charlestown, Massachusetts 02129

E-mail: vasilis@helix.mgh.harvard.edu

Abstract. As small animal optical imaging and tomography are gaining popularity for interrogating functional and molecular events *in vivo*, it becomes increasingly necessary to gain knowledge of the optical properties of the species investigated to better understand and describe photon propagation through their tissues. To achieve characterization of the spatial variation of average optical properties through murine chest cavities, time- and spatially resolved measurements of femto-second laser pulse transmission are performed through mice using a high-speed gated image intensifier. Application of time-resolved diffusion theory for finite slab geometry is first confirmed on phantoms and then applied to *in vivo* measurements for spatially resolving and quantifying mouse optical properties. Photon transmission images through mouse chest cavities are further obtained at different time gates to visualize the spatial variation observed and confirm the optical coefficient patterns calculated. © 2006 Society of Photo-Optical Instrumentation Engineers. [DOI: 10.1117/1.2400702]

Keywords: optical properties; diffusion theory; time-resolved measurements; femtosecond; *in vivo*.

Paper 06118R received May 9, 2006; revised manuscript received Jul. 17, 2006; accepted for publication Aug. 1, 2006; published online Nov. 30, 2006.

1 Introduction

The increasing use of animals in basic research and drug discovery has driven the need for improved imaging systems.¹ *In vivo* fluorescence optical imaging opens the possibility of interrogating cellular and subcellular bulk events through entire animals and has the advantage of utilizing nonionizing radiation and stable fluorochromes that can impart significant molecular specificity.² Quantification of absolute optical properties in intact mice is important for understanding mouse optical heterogeneity as is necessary for better describing photon propagation in tissue and improving inversion schemes in tomographic reconstructions.³

Study of the spatially and temporally resolved (or frequency domain) transmission of photons propagating through animals can enable quantification of optical properties, i.e., the absorption and reduced scattering coefficients.^{4–10} The use of time-resolved diffusion theory in modeling photon propagation to yield optical properties in homogeneous turbid media has been described in the literature in both diffuse reflectance (semi-infinite media) and transmission (finite slab) geometries. This has also allowed quantification of the average optical properties of generally heterogeneous tissues both *ex vivo* and *in vivo* by using the simplifying assumption that tissues are homogeneous for the volume probed by the optical measurement. For example, Patterson, Chance, and Wilson⁴ used diffuse reflectance measurements on human muscle at

630 nm and obtained an estimate for the reduced scattering coefficient (μ'_s) of 8.5 cm^{-1} and the absorption coefficient (μ_a) of 0.176 cm^{-1} . Tromberg et al.⁸ used frequency domain measurements at 674 nm to obtain values of $\mu'_s = 11 \text{ cm}^{-1}$ and $\mu_a = 0.04 \text{ cm}^{-1}$ in the human breast. Pifferi et al. and Torricelli et al.^{9,10} characterized the near-infrared optical properties of several human tissues including the breast ($\mu'_s \sim 5$ to 15 cm^{-1}) and abdomen ($\mu_a \sim 0.15$ to 0.35 cm^{-1}) using time-resolved measurements and the best fit to an analytical solution of a random walk model through a homogeneous slab. Other authors have reported similar values at near-infrared wavelengths.^{11–13}

While the optical coefficients of human tissues *in vivo* are now well studied, there is very little corresponding characterization of optical properties in small animals. The mouse torso in particular presents an optically complex model, because multiple organs with significantly different anatomy and function (e.g., the lung, heart, kidneys, and liver) are in close proximity to each other. In this work, we utilize a high-speed gated imaging system and femto-second laser source, combined with time-resolved diffusion theory in transmission mode to quantify spatially varying bulk optical properties. We first validate the approach with optical phantoms and then apply it to the study of mice *in vivo*. The theory employed is defined for homogeneous slabs of finite thickness; therefore, its application herein obtains average optical properties sampled along preferential photon paths through phantoms and animals. Using this approach, we further generate composite images of photon propagation through animals at dif-

Address all correspondence to Mark Niedre, Lab for Bio-Optics and Molecular Imaging, Center for Molecular Imaging Research Massachusetts General Hospital, Harvard Medical School, Building 149, 13th Street Room 5406 - Charlestown, MA 02129-2060; Tel: 617-726-5788; Fax: 617-726-5708; E-mail: mniedre@partners.org

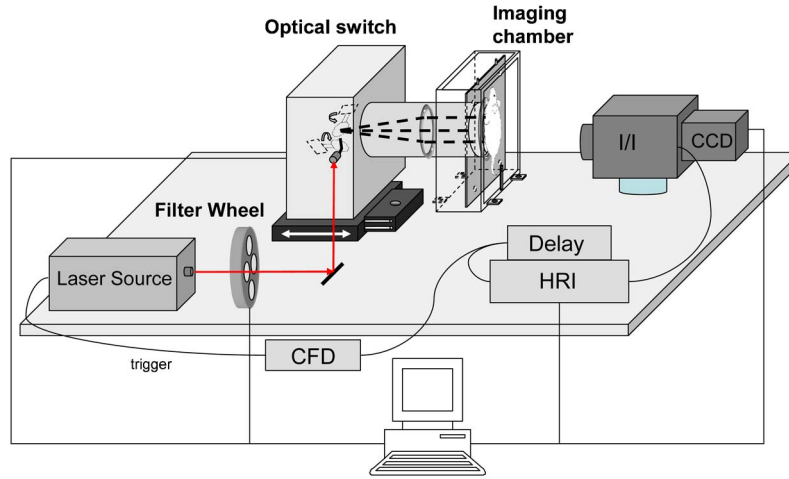


Fig. 1 Schematic of the time-resolved system. Samples were placed in the imaging chamber and compressed to 1.3 cm during transillumination: CFD, constant fraction discriminator; HRI, high rate imager; I/I, image intensifier.

ferent time gates to enable visualization of the optical variation.

2 Materials and Methods

2.1 Theory

Time-resolved diffusion theory through a homogeneous, turbid, finite-slab geometry has been described in detail in the literature.^{4,14} This theory utilizes the time-dependent diffusion equation, i.e.:

$$\frac{1}{c} \frac{\partial}{\partial t} \phi(\mathbf{r}, t) - D \nabla^2 \phi(\mathbf{r}, t) + \mu_a \phi(\mathbf{r}, t) = S(\mathbf{r}, t), \quad (1)$$

where c is the speed of light in tissue, D is the diffusion coefficient:

$$D = \{3[\mu_a + (1 - g)\mu_s]\}^{-1}, \quad (2)$$

μ_a is the absorption coefficient, μ_s is the scattering coefficient, g is the mean cosine of the scattering angle, and $S(\mathbf{r}, t)$ is the photon source. For the present work, the photon source is a femtosecond laser producing a very short (~ 100 fs) laser pulse collimated in a narrow (< 1 mm diam) pencil beam. In this case, a common approach to account for the influence of boundaries is to set the diffuse fluence to zero at an extrapolated boundary some distance z_b from the physical boundary of the slab. In this work, we have made the simplifying assumption that $z_b = 0$, i.e., the zero boundary condition (ZBC). Using this assumption, Patterson, Chance, and Wilson showed that the time-resolved transmission through a finite, homogeneous slab of turbid media can be analytically calculated when assuming an isotropic source as:⁴

$$T(\rho, d, t) = (4\pi Dc)^{-3/2} t^{-5/2} \exp(-\mu_a ct) \exp\left(-\frac{\rho^2}{4Dct}\right) \times \left\{ (d - z_o) \exp\left[-\frac{(d - z_o)^2}{4Dct}\right] - (d + z_o) \exp\left[-\frac{(d + z_o)^2}{4Dct}\right] \right\}, \quad (3)$$

where t is the time elapsed from the laser pulse launch in the medium and ρ is the radial distance from the point of entry of the laser in the medium. Previous studies have suggested that use of the mathematically more complex extrapolated boundary condition (EBC) would yield similar optical parameters for the experimental conditions used in this study.^{15,16} Furthermore, we have found that including both time and spatial profiles in our fitting algorithm significantly stabilizes the measurements and the reproducibility of the results.

2.2 Instrumentation

The system used for the time-resolved measurements has been described in detail previously¹⁷ and is shown in Fig. 1. Briefly, a femto-second laser (MaiTai, Spectra-Physics, Mountain View, California) operating at 732 nm with a pulse-width of approximately 100 fs was coupled to a scanning galvanometer. The laser light could be scanned in a noncontact manner across a sample placed in the imaging chamber as desired. The transmitted light was detected with a Cooke SensiCamQE charge-coupled device (CCD camera coupled with a gated image intensifier (LaVision Picostar HR12, LaVision GmbH, Goettingen, Germany)). A high-rate imager (Kentech Instruments Limited, Oxfordshire, England) and a picosecond delay unit (Kentech) allowed the acquisition of images with gate widths of 200 ps with a temporal step size of 25 ps.

In this setup, the laser was coupled to the imaging system via free-beam delivery using a set of two galvanometer-controlled mirrors and focusing lens for noncontact free beam scanning. A programmable ND filter wheel was placed in the path of the laser so that the incident power could be dynamically adjusted based on the attenuation of the sample using a feedback loop.

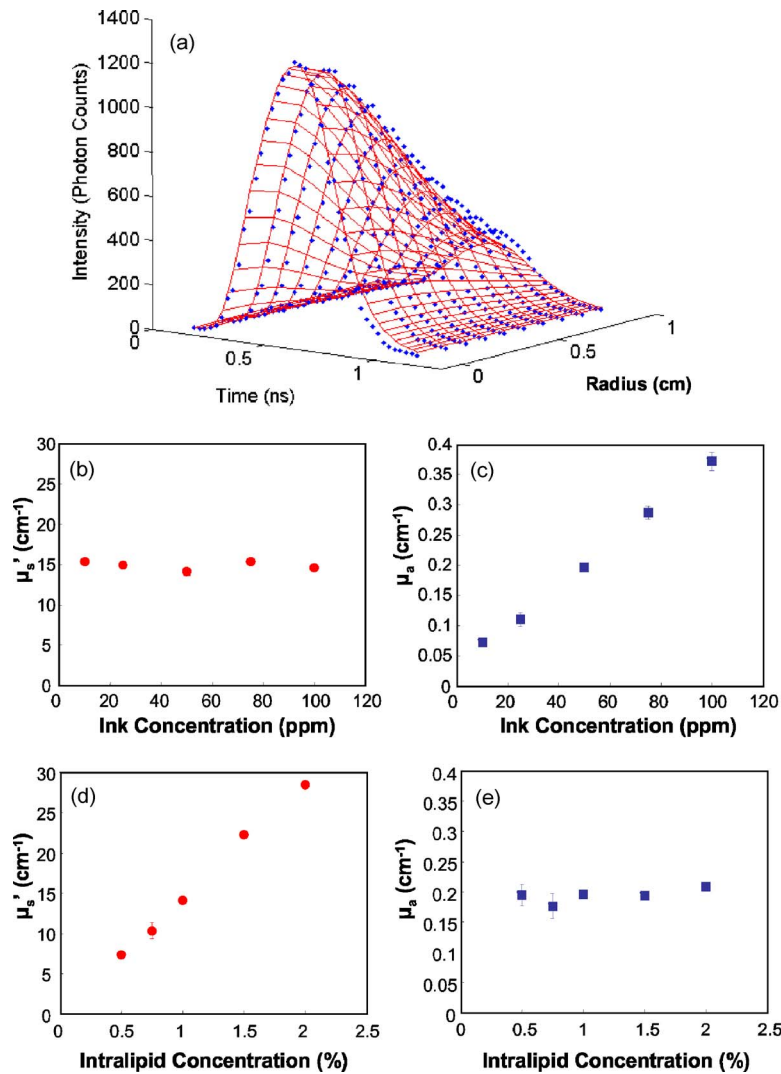


Fig. 2 Homogeneous optical phantoms. (a) Measured transmitted temporal and spatially resolved intensity (solid points) along with best fit (mesh surface) to time-resolved diffusion theory. Fitted values of (b) μ'_s and (c) μ_a as a function of increasing ink concentration. Fitted values of (d) μ'_s and (e) μ_a as a function of increasing intralipid concentration.

2.3 Data Collection and Analysis

The gated ICCD camera acquired photon profiles using a 200 ps gate with a step of 25 ps, resulting typically in acquiring 40 to 60 time gates. In this way, complete time-resolved images were obtained at each laser source position. The camera exposure was set to acquire for 1.6×10^7 laser pulses (i.e., 200 ms) at each time gate. The images were then analyzed to yield multiple photon profiles as a function of time and radial position from the source. The impulse response function of the system (measured independently) was then deconvolved from the signal using a commercial software package (Matlab, The Mathworks Incorporated, Natick, Massachusetts) to yield the true time and spatially resolved curves for each dataset. Equation (3) was then fit to the data using a nonlinear fitting routine to yield μ'_s and μ_a .

2.4 Homogeneous Phantoms

Two sets of homogeneous liquid solutions were prepared from a stock solution of 10% intralipid (Baxter Healthcare Corpo-

ration, Deerfield, Illinois) and ink (Higgins Ink, Sanford Corporation, Bellwood, Illinois) added, modifying the scattering and absorbing properties of the solutions, respectively. The final concentrations used were: 1. 1% intralipid with 10, 25, 50, 75, and 100 parts per million ink, and 2. 50-ppm ink with 0.5, 0.75, 1.0, 1.5, and 2% intralipid. The chamber length was set to 1.3 cm. Time-resolved images were acquired at five laser positions across the imaging chamber, and μ'_s and μ_a were determined by fitting to diffusion theory over a 1-cm radius from each source position. All experiments were repeated in triplicate.

2.5 Heterogeneous Phantoms

To verify that our system was capable of resolving spatially varying optical properties, a heterogeneous phantom was constructed. Two resin blocks ($5 \times 5 \times 1.3$ cm) were made from a mixture of clear acrylic resin (Casting Resin, Environmental Technologies Incorporated, Fields Landing, California), titanium dioxide (TiO₂; Sigma-Aldrich, Milwaukee, Wisconsin)

and ink (Sanford). The purpose of the titanium dioxide and ink pigment were to alter the scattering and absorption properties of the phantoms, respectively. The optical properties of the solid blocks were measured using the present technique and then cut into ~ 5 -mm-thick slabs and reassembled as a multilayer phantom model.

The heterogeneous phantom was then placed into the imaging chamber and the chamber length was set to 1.3 cm as before. Liquid solution (1% intralipid and 50 ppm of ink added) was added to the chamber to fill any small (submillimeter) gaps between the layers of the phantom and protect the intensified CCD. Hence, the intralipid contributed only a very small volume to the field of view and therefore had negligible effect on the optical property measurements. Full time-resolved scans were made at each of 104 points across the sample, arranged in eight rows of 13 source positions, separated by approximately 2 mm in the x direction and 3 mm in the y direction. The radius over which the diffusion theory was fit to the data was reduced from 1 cm to 3 mm for these experiments, since the larger radius of fitting completely obscured the phantom's heterogeneity.

2.6 In Vivo Mouse Studies

A total of five female nu/nu mice aged 4 to 6 weeks were used. Mice were placed under general anesthesia and then placed in the imaging chamber for either coronal or sagittal projections. The chamber was compressed to 1.3 cm and then filled with liquid matching solution containing 2% intralipid and 100 ppm of ink. The optical properties of the liquid used here were determined to represent the approximate average mouse optical properties. The mouse position and scanning pattern were adjusted so that the chest cavity was transilluminated in all cases. Since the compressed mouse occupied the entire 1.3-cm chamber length, the matching fluid was therefore only visible on the edges of the scanning area. As before, a total of 104 laser source positions were used for the *in vivo* experiments and diffusion theory was fit over a 3-mm radius from the center of each source position.

Two of the mice were euthanized by CO₂ asphyxiation after optical scanning. MRI scans were then performed (Bruker Pharmascan, 4.7T; Bruker BioSpin MRI Incorporated, Billerica, Massachusetts), so that the optical properties could be compared to anatomical features of the mice.

3 Results and Discussion

3.1 Homogeneous Phantoms

Homogeneous liquid phantoms with varying quantities of intralipid and ink were first analyzed with the system. Example intensity data as a function of radius and time for a solution with 1% intralipid and 50 parts per million ink are shown as solid points in Fig. 2(a). The best fit to Eq. (3) is also shown in Fig. 2(a) as the mesh surface. Note that the data here are the mean intensity over concentric circles of given radii from the center of the source position. Hence, the radial data are averaged over all angular directions and are therefore relatively noise-free. Use of both variables (radius and time) assisted in stabilization of the nonlinear fitting routine and calculation of accurate and reproducible parameters. The concentration of ink was then varied while maintaining a con-

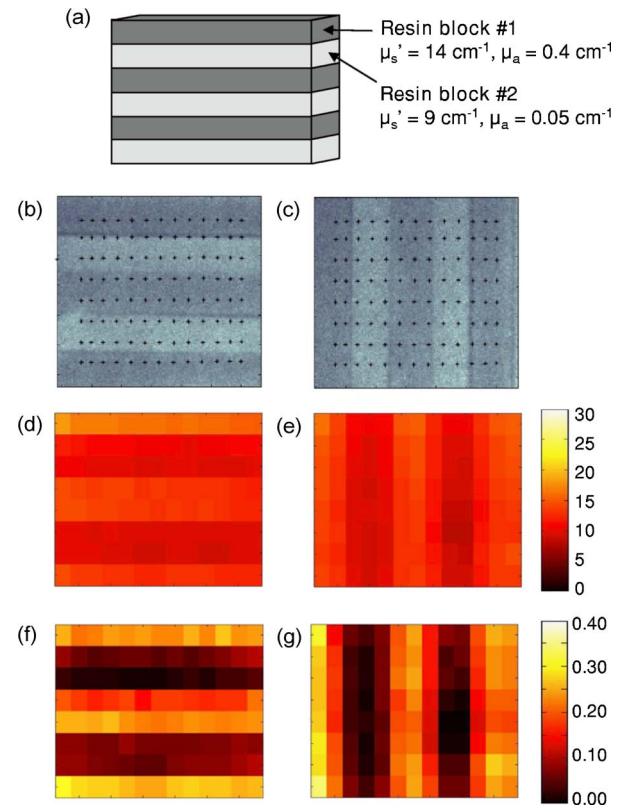


Fig. 3 Heterogeneous phantom experiments. (a) Diagram of layered optical phantom composed of two resin blocks with different optical properties. White light images of the phantom in (b) horizontal and (c) vertical orientations, along with the position of laser scan points (black dots). Fitted values of (d) and (e) μ'_s and (f) and (g) μ_a in both orientations. Scale bars are in cm^{-1} .

stant intralipid concentration. The resulting values for μ'_s and μ_a are shown in Figs. 2(b) and 2(c). Our value here of $\mu'_s = 15 \pm 0.5 \text{ cm}^{-1}$ for 1% intralipid is in reasonable agreement with the value of $\mu'_s = 11 \text{ cm}^{-1}$ at 730 nm reported by van Staveren et al.¹⁷ considering the very different technique used. Similarly, the concentration of intralipid was varied while maintaining a constant ink concentration, and the fitted values for μ'_s and μ_a are shown in Figs. 2(d) and 2(e). As can be seen, μ'_s and μ_a increase linearly with increasing intralipid and ink concentrations, respectively, while the unperturbed quantity remains constant. Likewise, our value here of $\mu_a = 0.19 \pm 0.1 \text{ cm}^{-1}$ for Higgins ink at a concentration of 50 ppm is in good agreement with the value of $\mu_a = 0.215 \text{ cm}^{-1}$ at 730 nm reported by Dimofte, Finlay, and Zhu.¹⁸ This verified that the time and spatially constrained approach combined with the selected time-resolved diffusion theory was capable of accurately measuring optical properties in homogeneous optical phantoms.

3.2 Heterogeneous Phantoms

To further confirm the accuracy of the method in optically heterogeneous media, two solid resin-based phantom blocks ($5 \times 5 \times 1.3 \text{ cm}$) were made with different quantities of TiO₂ and ink added. The optical properties measured from the resin blocks were found to be $\mu'_{s1} = 14 \text{ cm}^{-1}$, $\mu_{a1} = 0.4 \text{ cm}^{-1}$, and

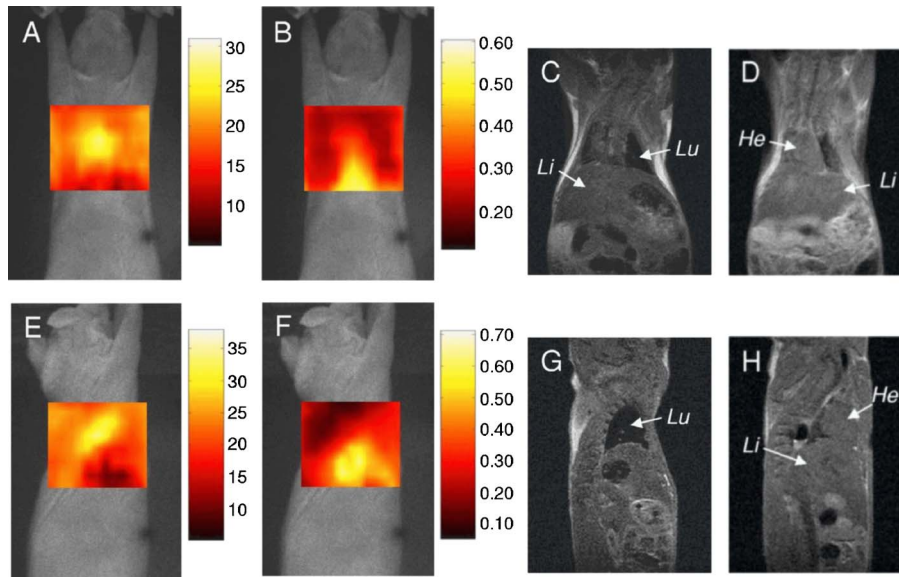


Fig. 4 Optical property maps obtained by transilluminating the chest cavity of mice. Fitted values of (a) μ'_s and (b) μ_a in the coronal projection, and (e) and (f) in the sagittal projection overlaid and interpolated onto the white-light image obtained by the system. MRI images showing the location of anatomical features in the (c) and (d) coronal and (g) and (h) sagittal projections at different depths. Major organs are labeled lung (Lu), liver (Li), and heart (He). Scale bars are in cm^{-1} .

$\mu'_{s2}=9 \text{ cm}^{-1}$, $\mu_{a2}=0.05 \text{ cm}^{-1}$. The two resin blocks were then cut and reassembled into a multilayer phantom as shown in Fig. 3(a). Figures 3(b) and 3(c) show white light images of the phantom in horizontal and vertical orientation, as well as the position of the laser scan points. Figures 3(d) and 3(e) show the values for μ'_s obtained and Figs. 3(f) and 3(g) show the values of μ_a obtained by fitting to the transmitted time-resolved curves measured in the experiment. The mean values of μ'_{s1} and μ_{a1} (i.e., the layers composed of the first phantom) obtained were 13.1 and 0.3 cm^{-1} , respectively, and for μ'_{s2} and μ_{a2} were 11.2 and 0.1 cm^{-1} , respectively. As might be expected, the optical properties from the different layers were somewhat “smeared” together (i.e., the measured optical properties from region 1 were lower than their true values), and those from region 2 were higher than their true values), since the 3-mm radius of fitting generally included more than one layer. Nevertheless, this experiment demonstrates the ability of this technique to measure average heterogeneous optical properties with good accuracy using a theory specified for homogeneous slabs.

3.3 In Vivo Mice Models

Time-resolved scans were then performed on a total of five nude mice. Figures 4(a) and 4(b) show examples of the fitted optical properties of mice in the coronal projection, overlaid on the white-light image obtained with the system. For visualization purposes, the measured optical properties have been overlaid on the positions of the laser scan points, and then interpolated to create an optical property map. Figures 4(c) and 4(d) show two coronal MRI slices obtained at different depths, showing the location of the heart, lung, and liver. Similarly, Figs. 4(e)–4(h) show the optical properties and MRI slices obtained at different depths in sagittal projection.

By comparing the anatomical information from the MRI scans to the optical property maps, estimates of the range of

optical properties of individual organs *in vivo* can be obtained. Table 1 summarizes these findings. As expected, the absorption coefficients of the heart and liver regions were high due to the large blood content of both organs. The reduced scattering coefficient of the lungs was also high as anticipated due to the multiple air-tissue interfaces in the alveoli. In general, the values obtained agree well with published values from the literature. For example, Beek et al.¹¹ reported a value for μ'_s of 20 cm^{-1} in lung, which is in reasonable agreement with our estimated range of 25 to 35 cm^{-1} . It should be reiterated that the values reported here are *in vivo* measurements as opposed to optical property measurements on excised tissue. Therefore, the lungs were inflated with air during the measurements, which likely increased optical scattering due to the presence of many small air-tissue interfaces. In addition, the measured values were consistent through all five of the mice investigated.

Finally, images of the photon transmission through the mice at different times were generated by combining small regions of interest ($2 \times 3 \text{ mm}$ rectangular) centered around the source position for each full-time curve and replotting them on single, composite images at each time gate. Figure 5(a) shows an example full-time curve of the mean intensity transmitted through a mouse *in vivo* as a function of time.

Table 1 Range of *in vivo* optical properties obtained and the corresponding anatomical features observed with MRI imaging.

	$\mu_a(\text{cm}^{-1})$	$\mu'_s(\text{cm}^{-1})$
Liver region	0.4 to 0.6	10 to 15
Lung region	0.2 to 0.3	25 to 35
Heart region	0.3 to 0.4	20 to 25

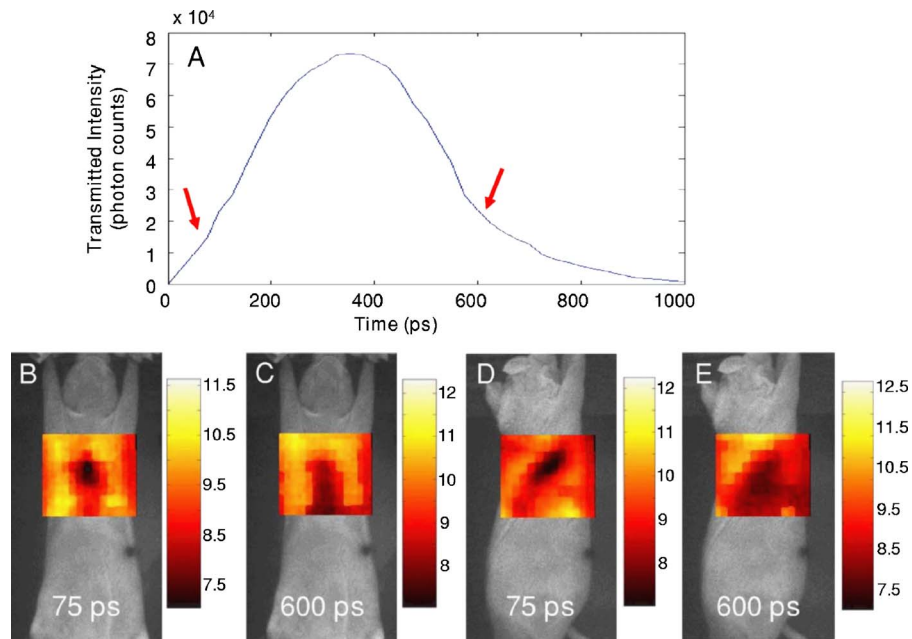


Fig. 5 Imaging of photon propagation through the chest cavity at different time gates. (a) Typical full-time curve through the chest cavity. Composite image of the natural logarithm of photons collected at an early (75 ps) time gate following the laser pulse for the (b) coronal and (d) sagittal projections. Composite image of photons collected at a later (600 ps) time gate for the (c) coronal and sagittal projections.

Figure 5(b) is a composite image of the photon transmission at an early time gate (75 ps) in the coronal projection. Similarly, Fig. 5(c) is a composite image of the photons transmitted at a later time gate (600 ps). Similarly, Figs. 5(d) and 5(e) are composite images of the photons transmitted at early and later time gates for the sagittal projection.

3.4 Discussion

While several optical properties for small animals have been published in the literature,¹² most reported observations are obtained *ex vivo* using excised tissues. However, optical properties may significantly change between *in vivo* and *ex vivo* observations due to structural changes and abrupt perturbation of physiological conditions, blood and water concentration, and overall hemodynamics.

Similar to the studies and the rationale behind work characterizing human tissues,^{6–10} we characterized the spatially dependent optical heterogeneity of mice as related to whole body imaging of the torso of small animals. We opted for characterizing average optical properties through mouse chest cavities using a time- and spatially dependent photon profiles yielding accurate and reproducible calculations. While the finite-slab time-resolved diffusion theory used in this analysis is specified for homogenous media,⁴ we further confirmed that this method can be applied in characterizing heterogeneous media with good accuracy. The experiments with heterogeneous phantoms successfully demonstrated that multiple layers could be resolved, and that diffusion theory yields average optical properties through the slab. While tomographic methods can be utilized to characterize the 3-D distribution of optical properties with improved resolution, such solutions are generally less accurate than the methodology selected here, due to the increased ill-posed nature of inverse diffuse optical tomography problems.

Therefore, this study favored accuracy and solution stability by calculating average optical properties through the mouse torso and by including relatively large radial distances (3 mm) into the spatially dependent fitting routine in exchange for resolution and the ability to separate layered structures. Reduction of the radius of fitting to 1 mm in an attempt to increase the resolution of the system resulted in destabilization of the fitting algorithm and significantly worse performance in terms of reproducibility and overall accuracy. Hence, the 3-mm fitting radius used in the heterogeneous phantom and *in vivo* experiments was empirically found to be the best compromise between ensuring optimal stability and maximum 2-D resolution.

This technique enabled quantification of the spatial variation of optical properties in whole mice *in vivo*. The values reported were averaged over the entire volume sampled by the transillumination measurements employed, and contain contributions of several tissue types. However, as confirmed by the calculated and measured images of Figs. 4 and 5, respectively, and the corresponding MRI images, there is generally good agreement between the spatial distribution seen and major underlying organs such as the heart, liver, and lungs that occupy a significant part of the volume sampled in the corresponding measurements. Of note is the reduced scattering coefficient calculated for the areas corresponding to the lung and heart, which appear relatively high compared to the other structures and previously published values for human or animal tissues. This value is, however, supported by the observed profiles of the transmitted photons through the mouse at early time gates [Figs. 5(b) and 5(d)]. As predicted by time-resolved diffusion theory⁴ and as noted in earlier work,^{19–21} the contrast observed in photon attenuation at early time gates correlates well with μ'_s . (As might be expected, the contrast in the time gate at 600 ps where the photons were more diffuse

appears to correspond to both μ'_s and μ_a .) It should also be noted that this value for μ'_s is the weighted average of the optical properties through the mouse, and therefore other nearby anatomical features in this region, such as the aortic/superior vena cava and pulmonary and coronary arteries or the highly curved area of the spinal cord, will influence the measured optical properties.

Overall, two- to three-fold spatial variation in optical coefficients was observed across small animal (murine) torsos. Practically, this means that light transmitted through 1 to 2 cm of the murine torso tissue will experience more than 2 orders of magnitude of variability in attenuation. Such heterogeneity, if not sufficiently accounted for, may lead to significant quantification errors and artifacts in fluorescence and bioluminescence imaging and tomography applications. We have recently reported experimental results that demonstrate how such high heterogeneity can be effectively accounted for in inverse diffuse optical tomography problems using the normalized Born approximation.²² Several other methods using a two-step solution of the coupled diffusion equations for light propagation in the excitation and emission wavelengths have been also proposed to tackle optical property variation in diffuse media.^{23,24}

Overall, the absolute optical properties through the mouse upper torso were calculated and the corresponding 2-D images of the spatial variation observed were obtained. These images correlated spatially with anatomical features of the mice, and the findings were further corroborated by images of photon transmission at individual time gates obtained through identical geometries.

Acknowledgments

This research was supported in part by National Institutes of Health grant RO1 EB 000750. The authors wish to acknowledge the contribution of Giannis Zacharakis in the original design of the instrument and Nooshin Hosseini in phantom preparation. Niedre acknowledges support from the National Cancer Institute of Canada through the Terry Fox Foundation.

References

1. V. Ntziachristos, J. Ripoll, L. V. Wang, and R. Weissleder, "Looking and listening to light: the evolution of whole-body photonic imaging," *Nat. Biotechnol.* **23**, 313–320 (2005).
2. V. Ntziachristos, E. A. Schellenberger, J. Ripoll, D. Yessayan, E. Graves, A. Bogdanov Jr., L. Josephson, and R. Weissleder, "Visualization of antitumor treatment by means of fluorescence molecular tomography with an annexin V-Cy5.5 conjugate," *Proc. Natl. Acad. Sci. U.S.A.* **101**, 12294–12299 (2004).
3. A. P. Gibson, J. C. Hebden, and S. R. Arridge, "Recent advances in diffuse optical imaging," *Phys. Med. Biol.* **50**, R1–R43 (2005).
4. M. S. Patterson, B. Chance, and B. C. Wilson, "Time resolved reflectance and transmittance for the non-invasive measurement of tissue optical properties," *Appl. Opt.* **28**, 2331–2336 (1989).
5. A. Kienle and M. S. Patterson, "Improved solutions of the steady-state and the time-resolved diffusion equations for reflectance from a semi-infinite turbid medium," *J. Opt. Soc. Am. A Opt. Image Sci. Vis* **14**, 246–254 (1997).
6. M. Gurfinkel, T. Pan, and E. M. Sevick-Muraca, "Determination of optical properties in semi-infinite turbid media using imaging measurements of frequency-domain photon migration obtained with an intensified charge-coupled device," *J. Biomed. Opt.* **9**(6), 1336–1346 (2004).
7. T. J. Farrell, M. S. Patterson, and B. Wilson, "A diffusion theory model of spatially resolved, steady-state diffuse reflectance for the noninvasive determination of tissue optical properties *in vivo*," *Med. Phys.* **19**, 879–888 (1992).
8. B. J. Tromberg, O. Coquoz, J. B. Fishkin, T. Pham, E. R. Anderson, J. Butler, M. Cahn, J. D. Gross, V. Venugopalan, and D. Pham, "Non-invasive measurements of breast tissue optical properties using frequency-domain photon migration," *Philos. Trans. R. Soc. London, Ser. B* **352**, 661–668 (1997).
9. A. Pifferi, P. Taroni, A. Torricelli, F. Messina, R. Cubeddu, and G. Danesini, "Four-wavelength time-resolved optical mammography in the 680–980-nm range," *Opt. Lett.* **28**, 1138–1140 (2003).
10. A. Torricelli, A. Pifferi, P. Taroni, E. Giambattistelli, and R. Cubeddu, "In vivo optical characterization of human tissues from 610 to 1010 nm by time-resolved reflectance spectroscopy," *Phys. Med. Biol.* **46**, 2227–2237 (2001).
11. J. F. Beek, H. J. van Staveren, P. Posthumus, H. J. Sterenborg, and M. J. van Gemert, "The optical properties of lung as a function of respiration," *Phys. Med. Biol.* **2**, 2263–2272 (1997).
12. W. F. Cheong, S. A. Prahl, and A. J. Welch, "A review of the optical-properties of biological tissues," *IEEE J. Quantum Electron.* **26**, 2166–2185 (1990).
13. V. Ntziachristos, X. H. Ma, A. G. Yodh, and B. Chance, "Multichannel photon counting instrument for spatially resolved near infrared spectroscopy," *Rev. Sci. Instrum.* **70**, 193–201 (1999).
14. F. Martelli, A. Sassaroli, Y. Yamada, and G. Zaccanti, "Analytical approximate solutions of the time-domain diffusion equation in layered slabs," *J. Opt. Soc. Am. A Opt. Image Sci. Vis* **19**, 71–80 (2002).
15. A. H. Hielscher, S. L. Jacques, L. Wang, and F. K. Tittel, "The influence of boundary conditions on the accuracy of diffusion theory in time-resolved reflectance spectroscopy of biological tissues," *Phys. Med. Biol.* **40**, 1957–1975 (1995).
16. R. C. Haskell, L. O. Svaasand, T. T. Tsay, T. C. Feng, M. S. McAdams, and B. J. Tromberg, "Boundary conditions for the diffusion equation in radiative transfer," *J. Opt. Soc. Am. A Opt. Image Sci. Vis* **11**, 2727–2741 (1994).
17. H. J. van Staveren, C. J. M. Moes, J. van Marle, S. A. Prahl, and M. J. C. van Gemert, "Light scattering in Intralipid-10% in the wavelength range of 400–1100 nm," *Appl. Opt.* **30**, 4507–4514 (1991).
18. A. Dimofte, J. C. Finlay, and T. C. Zhu, "A method for determination of the absorption and scattering properties interstitially in turbid media," *Phys. Med. Biol.* **50**, 2291–2311 (2005).
19. G. M. Turner, G. Zacharakis, A. Soubret, J. Ripoll, and V. Ntziachristos, "Complete-angle projection diffuse optical tomography by use of early photons," *Opt. Lett.* **30**, 409–411 (2005).
20. B. Chance, "Optical method," *Annu. Rev. Biophys. Biophys. Chem.* **20**, 1–28 (1991).
21. M. E. Zevallos, S. K. Gayen, B. B. Das, M. Alrubaiee, and R. R. Alfano, "Picosecond electronic time-gated imaging of bones in tissues," *IEEE J. Sel. Top. Quantum Electron.* **5**, 916–922 (1999).
22. A. Soubret, J. Ripoll, and V. Ntziachristos, "Accuracy of fluorescence tomography in the presence of heterogeneities: study of the normalized Born ratio," *IEEE Trans. Med. Imaging* **24**, 1377–1386 (2005).
23. A. B. Milstein, S. Oh, K. J. Webb, C. A. Bouman, Q. Zhang, D. A. Boas, and R. P. Millane, "Fluorescence optical diffusion tomography," *Appl. Opt.* **42**, 3081–3094 (2003).
24. M. J. Eppstein, D. J. Hawrysz, A. Godavarty, and E. M. Sevick-Muraca, "Three-dimensional, Bayesian image reconstruction from sparse and noisy data sets: near-infrared fluorescence tomography," *Proc. Natl. Acad. Sci. U.S.A.* **99**, 9619–9624 (2002).